

# Evidence for Recombining Plasma in the Supernova Remnant G346.6–0.2

Shigeo YAMAUCHI<sup>1</sup>, Masayoshi NOBUKAWA<sup>2</sup>, Katsuji KOYAMA<sup>2,3</sup>, and Manami YONEMORI<sup>3</sup>

<sup>1</sup>*Department of Physics, Faculty of Science, Nara Women's University, Kitauoyanishi-machi, Nara 630-8506*  
yamauchi@cc.nara-wu.ac.jp

<sup>2</sup>*Department of Physics, Graduate School of Science, Kyoto University,*  
*Kitashirakawa-oiwake-cho, Sakyo-ku, Kyoto 606-8502*

<sup>3</sup>*Department of Earth and Space Science, Graduate School of Science, Osaka University,*  
*1-1 Machikaneyama-cho, Toyonaka, Osaka 560-0043*

(Received 2012 May 29; accepted 2012 August 23)

## Abstract

We present the Suzaku results of the supernova remnant (SNR) G346.6–0.2. The X-ray emission has a center-filled morphology with the size of  $6' \times 8'$  within the radio shell. Neither an ionization equilibrium nor non-equilibrium (ionizing) plasma can reproduce the spectra remaining shoulder-like residuals in the 2–4 keV band. These structures are possibly due to recombination of free electrons to the K-shell of He-like Si and S. The X-ray spectra are well fitted with a plasma model in a recombination dominant phase. We propose that the plasma was in nearly full ionized state at high temperature of  $\sim 5$  keV, then the plasma changed to a recombining phase due to selective cooling of electrons to lower temperature of  $\sim 0.3$  keV. G346.6–0.2 would be in an epoch of the recombining phase.

**Key words:** ISM: individual (G346.6–0.2) — ISM: supernova remnants — X-rays: ISM — X-rays: spectra

## 1. Introduction

G346.6–0.2 is a supernova remnant (SNR) discovered in the radio band (Clark et al. 1975). The radio image shows a shell structure with the size of  $\sim 8'$  (Clark et al. 1975; Dubner et al. 1993; Whiteoak & Green 1996). Flux densities at 408 MHz, 843 MHz, 1.47 GHz, and 5 GHz were measured to be 14.9 Jy, 8.7 Jy, 8.1 Jy, and 4.3 Jy, respectively (Green 2009 and references therein), then the spectral index was estimated to be 0.5 (Clark et al. 1975; Green 2009). The SNR would be interacted with a molecular cloud because an OH maser was found (Green et al. 1997).

The Galactic plane survey project with ASCA discovered a faint X-ray emission from G346.6–0.2 for the first time (Yamauchi et al. 2008). The ASCA GIS image showed the diffuse X-ray morphology in the radio shell. The X-ray spectrum was represented by either a thermal plasma model with a temperature of  $\sim 1.6$  keV or a power-law model with a photon index of  $\sim 3.7$ . The absorption was as large as  $N_{\text{H}} = (2-3) \times 10^{22} \text{ cm}^{-2}$  (Yamauchi et al. 2008), which suggested that the SNR is located at a long distance, possibly in the Galactic inner disk or further. No further quantitative constraint was available with the ASCA data due to the limited photon statistics. G346.6–0.2 was then observed with Suzaku. Sezer et al. (2011) found strong emission lines of Si and S, and fitted the X-ray spectrum with a model of a power-law (photon index  $\sim 0.6$ ) plus a non-equilibrium ionization (NEI) (ionizing) plasma. They predicted that the strong Si and S lines are due to an ejecta-dominated plasma which origi-

nated from a Type Ia supernova explosion, and the power-law component is regarded as synchrotron emission.

Recently, strong radiative recombination continua (RRCs) have been discovered in the X-ray spectra of five mixed-morphology (MM) SNRs (Yamaguchi et al. 2009; Ozawa et al. 2009; Ohnishi et al. 2011; Sawada & Koyama 2012; Uchida et al. 2012). The RRC originates from radiative transitions of free electrons to the K-shell of ions, a sign of a recombination dominant plasma (RP). In the residuals of the NEI model fit for G346.6–0.2 in Sezer et al. (2011), we see a similar structure to the RRC.

G346.6–0.2 is located on the Galactic ridge, where a strong X-ray emission, called the Galactic Ridge X-ray Emission (GRXE), is prevailing. However, the previous data reduction and analyses did not properly take account of the GRXE as a major background for the faint and diffuse source. We, therefore, revisited the Suzaku data and performed the data reduction, spectral construction, and spectral analysis paying particular concerns on the subtraction of the GRXE. We then discovered evidence for the recombining plasma from this MM SNR for the first time.

## 2. Observation and Data Reduction

Suzaku (Mitsuda et al. 2007) carried out the Galactic center/plane mapping project with the CCD cameras (XIS, Koyama et al. 2007) placed at the focal planes of the thin foil X-ray Telescopes (XRT, Serlemitsos et al. 2007). The SNR G346.6–0.2 was observed on 2009 October 7–9 (Obs. ID 504096010). The pointing position was ( $l$ ,

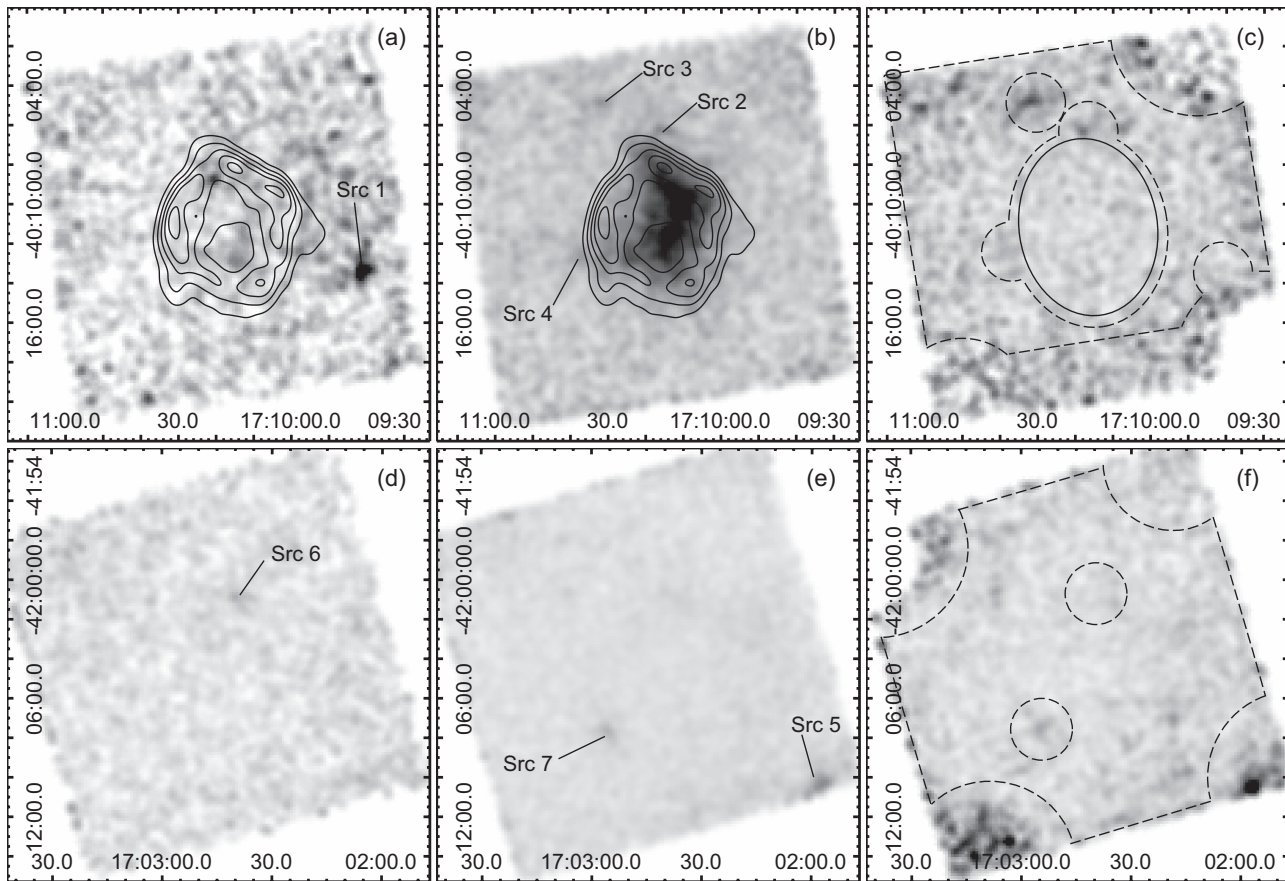


**Fig. 1.** Upper panel: XIS images of G346.6–0.2 in the 0.5–1 (a), 1–5 (b), and 5–8 keV (c) energy bands (gray scale). The coordinates are J2000.0. The radio map at 843 MHz using the Molonglo Observatory Synthesis Telescope (MOST) is displayed by the solid contours in (a) and (b) (Whiteoak & Green 1996). The X-ray images from XIS0, 1, and 3 were co-added. After the subtraction of the Non X-ray background (NXB), the vignetting corrections were made. The images were smoothed with a Gaussian distribution with the kernel of  $\sigma=24''$ . The intensity levels of the X-ray and radio bands are linearly spaced. Point-like sources are labeled as Src 1–Src 4. The background region (BGD-a) is shown by the dashed lines excluding the point-like sources (the dashed circles) in (c). The solid ellipse in (c) shows the source region. Lower panel: Same as (a)–(c), but the X-ray image of the background sky on a nearby source-free Galactic ridge. Src 5–7 are point-like sources. The background region (BGD-b) is shown by the dashed lines excluding the point-like sources (the dashed circles) in (f).

$b)=(346^{\circ}.63, -0^{\circ}.22)$ .

G346.6–0.2 is a faint X-ray SNR, located toward the inner Galactic disk. Therefore, the contribution of the GRXE, particular in the hard X-ray band above 5 keV, has a large impact on the source spectrum. Although the surface brightness of the GRXE is nearly constant along the Galactic plane within the range of a few degree of the Galactic longitude, the latitudinal variation is large, which is given by an exponential function with the scale height of  $\sim 0^{\circ}.5$  (e.g., Koyama et al. 1986; Yamauchi & Koyama 1993; Kaneda et al. 1997). We, therefore, selected two background regions for the spectrum of G346.6–0.2; one is the surrounding region of G346.6–0.2 in the same field of view (FOV) (hereafter BGD-a) and the other is a nearby region at  $(l, b)=(344^{\circ}.26, -0^{\circ}.22)$  (Obs. ID 502049010; hereafter BGD-b), at the same Galactic latitude but  $1^{\circ}$  away from G346.6–0.2 in longitude.

XIS sensor-1 (XIS1) is a back-side illuminated (BI) CCD, while the other three XIS sensors (XIS0, 2, and 3) are front-side illuminated (FI) CCDs. The FOV of the

XIS is  $17.8' \times 17.8'$ . Since one of the FIs (XIS2) turned dysfunctional in 2006 November<sup>1</sup>, we used the data obtained with the other CCD cameras (XIS0, 1, and 3). A small fraction of the XIS0 area was not used because of the data damage due possibly to an impact of micro-meteorite on 2009 June 23<sup>2</sup>. The XIS was operated in the normal clocking mode. The degraded spectral resolution due to the radiation of cosmic particles 4 years after the launch was restored by the spaced-row charge injection (SCI) technique. Details of the SCI technique are given in Nakajima et al. (2008) and Uchiyama et al. (2009).

Data reduction and analysis were made with the HEASoft version 6.11, SPEX (Kaastra et al. 1996) version 2.02.04, and the processed data version 2.4. The XIS pulse-height data for each X-ray event were converted to Pulse Invariant (PI) channels using the `xispi` software and the calibration database version 2011-11-09. We re-

<sup>1</sup> <http://www.astro.isas.ac.jp/suzaku/news/2006/1123/>

<sup>2</sup> <http://www.astro.isas.ac.jp/suzaku/news/2009/0702/>

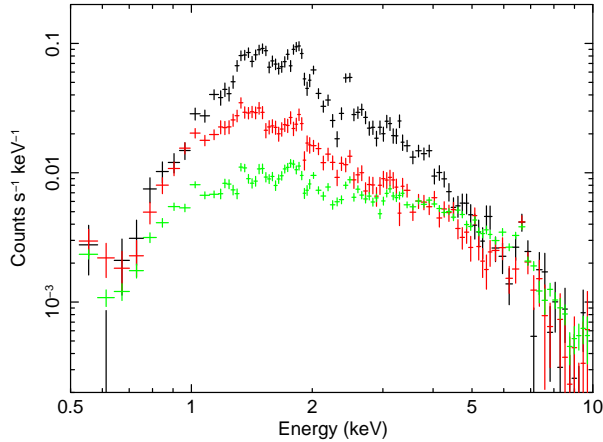


**Fig. 2.** Comparison of X-ray spectra of the source (black), the backgrounds of BGD-a (red), and BGD-b (green), after subtracting the NXB. Only the XIS0 data are plotted for brevity.

jected the data taken at the South Atlantic Anomaly, during the earth occultation, and at the low elevation angle from the earth rim of  $< 5^\circ$  (night earth) and  $< 20^\circ$  (day earth). The exposure times after these screenings were 56.8 and 215.7 ks for G346.6–0.2/BGD-a and BGD-b fields, respectively.

In the following data analysis, we subtracted the non-X-ray background (NXB), which was constructed from the night earth data generated by `xisnxbgen` (Tawa et al. 2008) in the HEASoft package.

### 3. Analysis and Results

#### 3.1. X-Ray Image

Figure 1 shows the vignetting corrected X-ray images for the G346.6–0.2/BGD-a (1a–1c) and BGD-b (1d–1f) fields, in the 0.5–1, 1–5, and 5–8 keV energy bands. The solid contours in figures 1a and 1b are the radio band image at the 843 MHz (Whiteoak & Green 1996). In order to increase X-ray photon statistics, we co-added all the data of XIS 0, 1, and 3. The images contain all the X-rays including the GRXE and the cosmic X-ray background (CXB). Above the X-ray fluxes of these backgrounds, diffuse X-rays from G346.6–0.2 are found only in the 1–5 keV band image (figure 1b); no significant X-ray is found in the 0.5–1 and 5–8 keV bands (figures 1a and 1c). We see a center-filled X-ray emission within the shell of the radio emission. In addition, four and three faint point-like sources are found in the G346.6–0.2 (Src 1–4) and BGD-b field (Src 5–7), respectively.

#### 3.2. X-Ray Spectra

The XIS spectra of G346.6–0.2, BGD-a, and BGD-b were extracted from the solid ellipse in figure 1c, the dashed lines in figures 1c, and 1f, respectively. For these data, we excluded regions of the point-like sources (Src 1–7) and the calibration sources at the field corners. The source and background spectra are shown in figure 2. The

hard X-ray flux above  $\sim 5$  keV is essentially comparable with each other, as is also noted in the hard X-ray band image of figure 1. The hard X-rays are likely due to the sum of the CXB and the GRXE. The Fe K-line emission at 6.7 keV is due to the GRXE, and the line intensities are also comparable between the source and two background spectra. We, therefore, conclude that after the subtraction of the proper background of the GRXE and the CXB, G346.6–0.2 should have no significant X-rays above  $\sim 5$  keV.

The BGD-a spectrum shows an X-ray excess over BGD-b in the low energy band below  $\sim 3$  keV. This implies that a local diffuse emission is prevailing around G346.6–0.2. We discuss this local diffuse emission in section 4.2. BGD-a should be a better background for G346.6–0.2 because of the close vicinity, but photon statistics are limited due to less exposure time of 56.8 ks and off-axis vignetting effect. BGD-b, on the other hand, provides better photon statistics due to longer exposure of 215.7 ks and larger correcting area than BGD-a. We, therefore, made two source spectra by the subtraction of each background, BGD-a or BGD-b. The exposure times and vignetting effects of these backgrounds were corrected by the method shown by Hyodo et al. (2008).

For the spectral analysis, the Response files, Redistribution Matrix Files (RMFs) and Ancillary Response Files (ARFs), were made using `xisrmfgen` and `xissimarfgen`, respectively, in the HEASoft package. The ARFs were created assuming the observed image to the photon distribution.

##### 3.2.1. G346.6–0.2

The spectra of G346.6–0.2 were made by subtracting BGD-a or BGD-b (here spectra-a and spectra-b, respectively). These spectra were separately given in figures 3a and 3f, respectively. For these spectra, we applied a thin thermal plasma model in collisional ionization equilibrium (CIE) (`vapex` model in XSPEC) modified by interstellar absorption (`wabs` model in XSPEC). The cross-sections of the photoelectric absorption were taken from Morrison & McCammon (1983), while the abundance data were taken from Anders & Grevesse (1989). The abundances of Mg, Si, S, Ar, and Fe were set to be free and those of Ca and Ni were assumed to be the same as Ar and Fe, respectively. The others were fixed to the solar values. The XIS 0, 1 and 3 spectra were simultaneously fitted. The 1-CIE model was rejected with the large  $\chi^2$  values of 354 and 423 (d.o.f.=193) for spectra-a and spectra-b, respectively. The best-fit parameters are listed in table 1, while the residuals from the best-fit model are plotted in figures 3b and 3g. We found systematic residuals (shoulder-like structures) in the 1.5–4 keV energy band. We further examined a plasma model in an NEI state (`vnei` model in XSPEC) to the source spectra and confirmed that the model was also rejected with the  $\chi^2$  values of 309 and 428 (d.o.f.=192) for spectra-a and spectra-b, respectively. The residuals were essentially similar to those of 1-CIE model. We note that similar shoulder-like structures are found in the NEI model fit of Sezer et al. (2011) (figure 3), although the data reduction process was different from

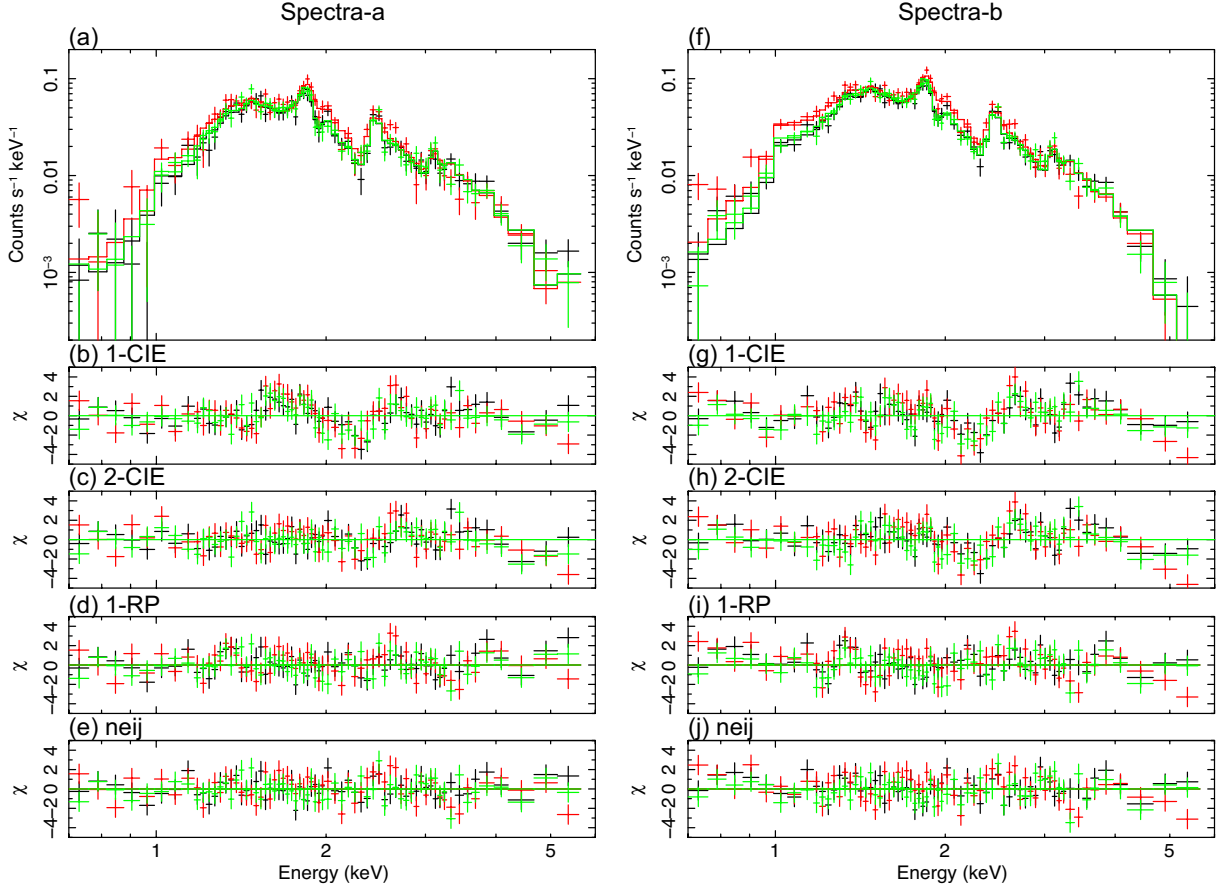


**Fig. 3.** X-ray spectra of G346.6–0.2 obtained with the Suzaku XIS and the residuals from the best-fit model (see text). The black, red, and green colors show XIS 0, 1, and 3 data, respectively. The left panels are the results of spectra-a (BGD-a subtracted spectra), while the right panels are those of spectra-b (BGD-b subtracted spectra). The histograms in (a) and (f) are the best-fit *neij* models (see table 1), while the residuals from the models of 1-CIE, 2-CIE, 1-RP and *neij* are shown in the histograms of (b), (c), (d) and (e) (for spectra-a), and (g), (h), (i) and (j) (for spectra-b), respectively.

the present paper.

We then applied a 2-component CIE plasma (2-CIE) model (2-*vapex* model), assuming the abundances of the two plasma components to be equal. This model was also rejected with the  $\chi^2$  values of 249 and 373 (d.o.f.=191) for spectra-a and spectra-b, respectively (table 1). The residuals from the best-fit model are plotted in figures 3c and 3h. The residuals in the 1.5–2 keV band disappeared, but those at the energy of 2–4 keV remained. These residuals show shoulder-like shapes with the leading edge energies of  $\sim 2.4$  keV and  $\sim 3.2$  keV which correspond the ionization energies of He-like Si and He-like S ions, respectively. The same features were also reported from IC443, G359.1–0.5, W28, and W44 (Yamaguchi et al. 2009; Ohnishi et al. 2011; Sawada & Koyama 2012; Uchida et al. 2012). These authors predicted that the residuals are due to the RRC which is a sign of the RP.

We, therefore, applied a *cie* model in the SPEX package (Kaastra et al. 1996) applying the *absm* model for the interstellar absorption. The *cie* model treats an electron temperature ( $kT_e$ ) and an ionization temperature ( $kT_z$ ) independently (here 1-RP model). The best-fit param-

eters are listed in table 1. Although the  $\chi^2$  value for spectra-b was significantly improved from 373 (d.o.f=191) to 306 (d.o.f=192), that for spectra-a was not improved (248 of d.o.f=192). Furthermore, the best-fit abundances of Ar and Ca are 4–5 solar, which is far higher than any other elements of solar or sub-solar abundances. The residuals from the best-fit 1-RP model are plotted in figures 3d and 3i. The residuals at 2–4 keV are partly reduced, but a new residual was appeared at the energy of  $\sim 1.35$  keV corresponding to the He-like Mg  $K\alpha$  line.

The additional excess from the He-like Mg  $K\alpha$  and unreasonable high abundances of Ar and Ca suggest that the single ionization-temperature (1- $kT_z$ ) plasma in the *cie* model is inadequate. In fact, Sawada & Koyama (2012) and Uchida et al. (2012) found that the spectra of MM SNRs, W28 and W44, have multi-ionization temperatures. They successfully predicted the multi-ionization temperature structure with a scenario that the X-ray emitting plasma is in a transition phase of recombining process. In order to examine a possibility of a multi- $kT_z$  plasma for G346.6–0.2, we fitted the spectra with the *neij* model in SPEX. The *neij* model describes a plasma state when the

**Table 1.** The best-fit parameters derived from a spectral analysis.\*

Parameter Model	Value			
	XSPEC: vapec 1-CIE	XSPEC: 2 vapec 2-CIE	SPEX: cie 1-RP	SPEX: neij
Spectra-a				
$N_{\text{H}}$ ( $\times 10^{22}$ cm $^{-2}$ )	$2.9^{+0.3}_{-0.4}$	$3.8^{+0.3}_{-0.5}$	$1.9^{+0.1}_{-0.1}$	$2.3^{+0.1}_{-0.1}$
$kT_{\text{e}}$ (keV)	$1.01^{+0.04}_{-0.04}$	$0.18^{+0.04}_{-0.02}$	$0.37^{+0.04}_{-0.03}$	—
	—	$1.19^{+0.15}_{-0.10}$	—	—
$kT_{\text{z}}/kT_{\text{e}}$	—	—	$2.9^{+0.4}_{-0.3}$	—
$kT_{\text{e}1}$ (keV)	—	—	—	5 (fixed)
$kT_{\text{e}2}$ (keV)	—	—	—	$0.30^{+0.03}_{-0.01}$
$n_{\text{e}}t^{\ddagger}$ ( $\times 10^{11}$ cm $^{-3}$ s)	—	—	—	$4.8^{+0.1}_{-0.4}$
Mg $^{\ddagger}$	$1.7^{+0.9}_{-0.6}$	$0.4^{+0.4}_{-0.3}$	$0.2^{+0.2}_{-0.2}$	$0.4^{+0.1}_{-0.2}$
Si $^{\ddagger}$	$1.1^{+0.8}_{-0.5}$	$1.7^{+1.0}_{-0.5}$	$0.8^{+0.1}_{-0.2}$	$0.6^{+0.2}_{-0.1}$
S $^{\ddagger}$	$1.3^{+0.5}_{-0.4}$	$2.7^{+1.1}_{-0.7}$	$1.4^{+0.2}_{-0.4}$	$0.6^{+0.3}_{-0.1}$
Ar $^{\ddagger}$ = Ca $^{\ddagger}$	$1.5^{+0.7}_{-0.6}$	$2.0^{+1.1}_{-0.8}$	$4.6^{+1.0}_{-2.0}$	$1.1^{+0.3}_{-0.3}$
Fe $^{\ddagger}$ = Ni $^{\ddagger}$	$3.3^{+3.5}_{-2.0}$	$4.5^{+6.1}_{-3.1}$	<0.01	<0.2
Others $^{\ddagger}$	1 (fixed)	1 (fixed)	1 (fixed)	1 (fixed)
$\chi^2/\text{d.o.f.}$	354/193	249/191	248/192	226/192
Spectra-b				
$N_{\text{H}}$ ( $\times 10^{22}$ cm $^{-2}$ )	$1.7^{+0.3}_{-0.2}$	$2.1^{+0.3}_{-0.3}$	$1.5^{+0.1}_{-0.1}$	$2.1^{+0.3}_{-0.1}$
$kT_{\text{e}}$ (keV)	$0.93^{+0.05}_{-0.03}$	$0.27^{+0.03}_{-0.05}$	$0.39^{+0.04}_{-0.02}$	—
	—	$1.00^{+0.06}_{-0.04}$	—	—
$kT_{\text{z}}/kT_{\text{e}}$	—	—	$2.8^{+0.3}_{-0.2}$	—
$kT_{\text{e}1}$ (keV)	—	—	—	5 (fixed)
$kT_{\text{e}2}$ (keV)	—	—	—	$0.30^{+0.05}_{-0.04}$
$n_{\text{e}}t^{\ddagger}$ ( $\times 10^{11}$ cm $^{-3}$ s)	—	—	—	$4.8^{+1.2}_{-0.1}$
Mg $^{\ddagger}$	$0.6^{+0.2}_{-0.1}$	$0.7^{+0.1}_{-0.2}$	$0.4^{+0.2}_{-0.2}$	$0.5^{+0.2}_{-0.2}$
Si $^{\ddagger}$	$0.4^{+0.1}_{-0.1}$	$0.5^{+0.2}_{-0.1}$	$0.8^{+0.2}_{-0.1}$	$0.6^{+0.1}_{-0.1}$
S $^{\ddagger}$	$0.8^{+0.2}_{-0.1}$	$1.0^{+0.2}_{-0.2}$	$1.5^{+0.4}_{-0.3}$	$0.6^{+0.1}_{-0.2}$
Ar $^{\ddagger}$ = Ca $^{\ddagger}$	$1.7^{+0.5}_{-0.4}$	$1.6^{+0.5}_{-0.4}$	$4.0^{+1.0}_{-1.5}$	$1.0^{+0.5}_{-0.3}$
Fe $^{\ddagger}$ = Ni $^{\ddagger}$	$0.2^{+0.3}_{-0.2}$	$0.2^{+0.3}_{-0.2}$	<0.01	$0.3^{+0.3}_{-0.2}$
Others $^{\ddagger}$	1 (fixed)	1 (fixed)	1 (fixed)	1 (fixed)
$\chi^2/\text{d.o.f.}$	423/193	373/191	306/192	268/192

\* Errors are estimated at the 90% confidence levels.

$^{\ddagger}$  Recombination timescale, where  $n_{\text{e}}$  is the electron density (cm $^{-3}$ ) and  $t$  is the elapsed time after the cooled down epoch (s).

$^{\ddagger}$  Relative to the solar value (Anders & Grevesse 1989).

initial plasma was in CIE with the temperature of  $kT_{\text{e}1}$ , then only the electron temperature dropped to  $kT_{\text{e}2}$  by a rapid electron cooling in the past. In the initial phase, the plasma was in  $1\text{-}kT_{\text{z}}$  plasma ( $kT_{\text{z}}=kT_{\text{e}1}$ ), then forced recombination as a function of  $n_{\text{e}}t$ , where  $n_{\text{e}}$  and  $t$  are an electron density and an elapsed time after the electron cool-down epoch, respectively. Since the time scale of recombination is element-dependent, the time evolution realizes a multi- $kT_{\text{z}}$  plasma.

The **neij** model gave better reduced  $\chi^2$  value than the simple 1-RP (**cie**) model with  $\Delta\chi^2 = 22$  (spectra-a) and 38 (spectra-b), but no constraint on  $kT_{\text{e}1}$  was obtained with the error ranges of  $>4$  keV and  $>3$  keV (90% con-

fidence level) for spectra-a and spectra-b, respectively. These error ranges mean that the initial plasma of  $kT_{\text{e}1}$  is in nearly full ionized state for all the relevant elements except for Fe (Fe would be in between full ionized and H-like states). Taking account of the initial plasma condition, we assumed  $kT_{\text{e}1}=5$  keV as a physically reasonable value and tried the final **neij** fitting. The best-fit parameters and the  $\chi^2$  values are listed in table 1. The best-fit model is plotted in figures 3a and 3f, while the residuals are shown in figures 3e and 3j. On the contrary to the simple 1-RP model, the **neij** model gave reasonable abundances of Ar and Ca similar to the other elements. Thus, we conclude that the overall spectra of G346.6–0.2 were nicely fitted

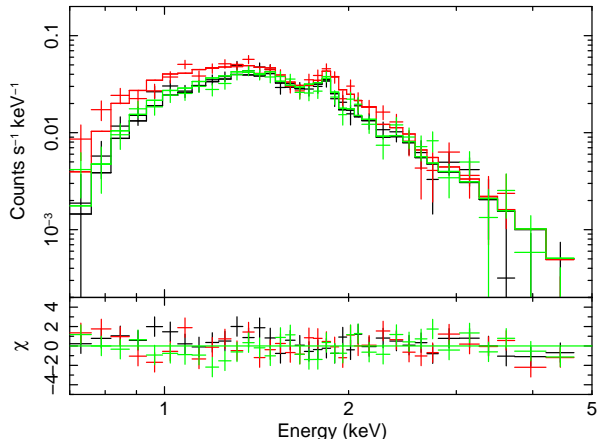


**Fig. 4.** An X-ray spectrum of an excess emission around G346.6–0.2. The black, red, and green colors show XIS 0, 1, and 3 data, respectively. The best-fit `apec` model is plotted by the solid histogram.

**Table 2.** The best-fit parameters derived from a spectral analysis for an excess emission around G346.6–0.2.\*

Parameter	Value
Model	XSPEC: <code>apec</code>
$N_{\text{H}}$ ( $\times 10^{22}$ cm $^{-2}$ )	$1.2^{+0.1}_{-0.2}$
$kT_{\text{e}}$ (keV)	$0.79^{+0.06}_{-0.05}$
Abundance $^{\dagger}$	$0.14^{+0.06}_{-0.04}$
$\chi^2/\text{d.o.f.}$	102/104

\* Errors are estimated at the 90% confidence levels.

$^{\dagger}$  Relative to the solar value (Anders & Grevesse 1989).

with the `neij` model.

### 3.2.2. Local Emission around G346.6–0.2

In the background estimation process, we found a local excess in soft X-rays around G346.6–0.2. The X-ray spectrum of this local excess emission was made by subtracting BGD-b from the BGD-a data (figure 2), which is given in figure 4. The X-ray spectrum shows a weak Si  $K\alpha$  line, which means a thin thermal origin. The spectrum was nicely fitted by a thin thermal plasma model, the `apec` in XSPEC, with  $\chi^2/\text{d.o.f.} = 102/104$ . The results are listed in table 2 and the best-fit model is plotted in figure 4.

## 4. Discussion

### 4.1. G346.6–0.2

For the background estimation, we took account of the difference of vignetting effects between the source and background regions. Furthermore, we tried two different backgrounds of BGD-a and BGD-b (spectra-a and spectra-b). Although the fluxes of these backgrounds are different, the spectral shapes are very similar. As the results, these two spectra, spectra-a and spectra-b, gave essentially the same best-fit parameters except for the ab-

solute luminosity. Since BGD-a and G346.6–0.2 are likely in a local soft X-ray excess around G346.6–0.2, we discuss based on the results of spectra-a, the BGD-a subtracted spectra.

The spectrum was nicely described by the RP in a transition epoch of its recombining phase (`neij` model). The best-fit electron temperature was about 0.3 keV. These conclusions are inconsistent with those of Yamauchi et al. (2008) and Sezer et al. (2011). In the thermal plasma fitting, their results were in CIE or NEI with the electron temperatures of  $\sim 1.6$  keV and 0.97–1.3 keV in Yamauchi et al. (2008) and Sezer et al. (2011), respectively. These apparent inconsistencies are mainly due to the background subtraction. Sezer et al. (2011) used the background from very small region (near the corner of the FOV), while Yamauchi et al. (2008) used the annulus region around the source. No vignetting effect was corrected in Yamauchi et al. (2008) and Sezer et al. (2011). Therefore, the background-subtracted spectra provide less statistics and should contain some fractions of the GRXE emission, particularly in the hard X-ray band. In fact, they reported that the X-ray spectrum has excess flux above  $\sim 5$  keV. This may artificially predict higher electron temperatures and/or power-law component.

Assuming the mean density of  $1\text{H cm}^{-3}$ , the derived  $N_{\text{H}}$  value of  $(2.3 \pm 0.1) \times 10^{22}$  cm $^{-2}$  corresponds to the distance of 7–8 kpc, which is well consistent with the distance of 8.2 kpc estimated from  $\Sigma$ - $D$  relation (Case & Bhattacharya 1998). If we assume the distance of 8 kpc, the luminosity was calculated to be  $3.5 \times 10^{35}$  erg s $^{-1}$  in the 0.5–10 keV energy band. The abundances are sub-solar to solar, which is consistent with those of Sezer et al. (2011). They predicted that the remnant may originate from a Type Ia supernova (SN) explosion, and the solar/sub-solar abundances of heavy elements are explained by the scenario that the SNR is young, and the reverse shock does not reach yet to the interior of the ejecta. Our best-fit  $n_e t$  is  $(4.8^{+0.1}_{-0.4}) \times 10^{11}$  cm $^{-3}$  s. Then, assuming the mean density of  $1\text{H cm}^{-3}$ , the age of G346.6–0.2 is estimated to be  $1.4 \times 10^4$ – $1.6 \times 10^4$  yr. This means that G346.6–0.2 is not a young SNR, and hence no evidence for the young Type Ia SN scenario is obtained. The solar/sub-solar abundances plasma would be mainly due to interstellar matter.

G346.6–0.2 is the sixth sample of the SNRs with the RP, after IC443 (Yamaguchi et al. 2009), W49B (Ozawa et al. 2009), G359.1–0.5 (Ohmishi et al. 2011), W28 (Sawada & Koyama 2012), and W44 (Uchida et al. 2012). Among these SNRs with the RP, the plasma structures in W28 and W44 were studied in detail. The results were that the RP is in a recombining phase of  $\sim 10^{11} (n_e/1\text{H cm}^{-3})^{-1}$  s after the production of the initial RP. We found that G346.6–0.2 is explained with a similar scenario as these SNRs. We propose that the other SNRs, IC443, W49B, and G359.1–0.5, can also be explained by the same scenario, a plasma in an epoch of recombining process.

All the previous RP-detected SNRs share some common characteristics: (1) they are classified to MM SNRs (Rho & Petre 1998), (2) an OH maser is detected, suggesting the interaction with molecular clouds, and (3) TeV/GeV

$\gamma$ -ray emission is detected. For possible origins of the RP based on these common features, one can refer the discussions in Yamaguchi et al. (2009), Sawada & Koyama (2012), and Uchida et al. (2012). The center-filled thermal X-ray emission within the radio shell suggests that G346.6–0.2 is a MM SNR. An OH maser has been found (Green et al. 1997), but no TeV/GeV  $\gamma$ -ray emission has been found from G346.6–0.2. Therefore, future TeV/GeV  $\gamma$ -ray search from this SNR is encouraged.

#### 4.2. Local Emission

The excess emission around G346.6–0.2 was shown by the optically thin thermal plasma with the temperature of 0.79 keV, 0.14 solar abundance, and  $N_{\text{H}}$  value of  $1.2 \times 10^{22}$   $\text{cm}^{-2}$ . The ASCA Galactic plane survey revealed that the GRXE spectra observed in various regions are well represented by an optically thin thermal plasma model with two temperatures of  $<1$  keV and  $\sim 7$  keV (Kaneda 1997; Kaneda et al. 1997). The two-temperature structure was confirmed by Chandra (Ebisawa et al. 2005) and Suzaku (Ryu et al. 2009). The spectral parameters of the excess emission in the G346.6–0.2 field are similar to those of the soft component of the GRXE. The intensity distribution of the hard component along the Galactic plane is symmetric with respect to the Galactic center, while that of the soft component is more asymmetric: a local peak and a local minimum were found at  $l \sim 347^\circ$  and  $l \sim 355^\circ$ , respectively (Kaneda 1997); the longitudinal distribution of the GRXE soft component shows that the intensity near the BGD-a region is about  $\sim 1.3$  times higher than that of the BGD-b region (Kaneda 1997). Our present result of BGD-a is  $\sim 2$  times larger than BGD-b in the soft X-ray band, and hence the excess would not be due to the fluctuation of the GRXE, but would be a local plasma. The  $N_{\text{H}}$  value of the local plasma is smaller than that of G346.6–0.2 in the GRXE, hence this emission is located at the near side of G346.6–0.2 and the GRXE. The local plasma is near to the direction of the non-thermal SNR RX J1713.7–3946 and the  $N_{\text{H}}$  value is similar to that of RX J1713.7–3946 (Koyama et al. 1997). Therefore, the local plasma is located near RX J1713.7–3946 at the distance of 1–2 kpc. Whether this thermal plasma is physically associated with RX J1713.7–3946 or not is unclear. To clarify this, we encourage further observations around RX J1713.7–3946.

We would like to express our thanks to all of the Suzaku team. We thank Dr. M. Sawada for his useful comments. This work was supported by the Japan Society for the Promotion of Science (JSPS); the Grant-in-Aid for Scientific Research (C) 21540234 (SY), 24540232 (SY), and 24540229 (KK), Young Scientists (B) 24740123 (MN), Challenging Exploratory Research program 20654019 (KK), and Specially Promoted Research 23000004 (KK).

#### References

- Anders, E., & Grevesse, N. 1989, *Geochim. Cosmochim. Acta*, 53, 197
- Case, G. L., & Bhattacharya, D. 1998, *ApJ*, 504, 761
- Clark, D. H., Caswell, J. L., & Green, A. J. 1975, *Australian Journal of Physics Astrophysical Supplement*, Sept., 1
- Dubner, G. M., Moffett, D. A., Goss, W. M., & Winkler, P. F. 1993, *AJ*, 105, 2251
- Ebisawa, K., et al. 2005, *ApJ*, 635, 214
- Green, D. A. 2009, *A Catalog of Galactic Supernova Remnants (2009 March version)*, (Astrophysics Group, Cavendish Laboratory, Cambridge, UK)<sup>3</sup>
- Green, A. J., Frail, D. A., Goss, W. M., & Otrupceck, R. 1997, *AJ*, 114, 2058
- Hyodo, Y., Tsujimoto, M., Hamaguchi, K., Koyama, K., Kitamoto, S., Maeda, Y., Tsuboi, Y., & Ezoe, Y. 2008, *PASJ*, 60, S85
- Kaastra, J. S., Mewe, R., & Nieuwenhuijzen, H. 1996, *UV and X-ray Spectroscopy of Astrophysical and Laboratory Plasmas*, ed. K. Yamashita and T. Watanabe (Universal Academy Press, Tokyo), p.411
- Kaneda, H. 2007, Ph.D. thesis, The University of Tokyo
- Kaneda, H., Makishima, K., Yamauchi, S., Koyama, K., Matsuzaki, K., & Yamasaki, N. Y. 2007, *ApJ*, 491, 638
- Koyama, K., Makishima, K., Tanaka, Y., & Tsunemi, H. 1986, *PASJ*, 38, 121
- Koyama, K., Kinugasa, K., Matsuzaki, K., Nishiuchi, M., Sugizaki, M., Torii, K., Yamauchi, S., & Aschenbach, B. 1997, *PASJ*, 49, L7
- Koyama, K., et al. 2007, *PASJ*, 59, S23
- Mitsuda, K., et al. 2007, *PASJ*, 59, S1
- Morrison, R., & McCammon, D. 1983, *ApJ*, 270, 119
- Nakajima, H., et al. 2008, *PASJ*, 60, S1
- Ohnishi, T., Koyama, K., Tsuru, T. G., Masai, K., Yamaguchi, H., & Ozawa, M. 2011, *PASJ*, 63, 527
- Ozawa, M., Koyama, K., Yamaguchi, H., Masai, K., & Tamagawa, T. 2009, *ApJ*, 706, L71
- Rho, J., & Petre, R. 1998, *ApJ*, 503, L167
- Ryu, S., Koyama, K., Nobukawa, M., Fukuoka, R., & Tsuru, T. G. 2009, *PASJ*, 61, 751
- Sawada, M., & Koyama, K., 2012, *PASJ*, in press
- Serlemitsos, P., et al. 2007, *PASJ*, 59, S9
- Sezer, A., Gök, F., Hudaverdi, M., Kimura, M., & Ecran, E. N. 2011, *MNRAS*, 415, 301
- Tawa, N., et al. 2008, *PASJ*, 60, S11
- Uchida, H., et al. 2012, submitted to *PASJ*
- Uchiyama, H., et al. 2009, *PASJ*, 61, S9
- Whiteoak, J. B. Z., & Green A. J. 1996, *A&AS*, 118, 329
- Yamaguchi, H., Ozawa, M., Koyama, K., Masai, K., Hiraga, J., Ozaki, M., & Yonetoku, D. 2009, *ApJ*, 705, L6
- Yamauchi, S. & Koyama, K. 1993, *ApJ*, 404, 620
- Yamauchi, S., Ueno, M., Koyama, K., & Bamba, A. 2008, *PASJ*, 57, 459

<sup>3</sup> <http://www.mrao.cam.ac.uk/surveys/snrs/>